

## Impact of wavefront shape on nonlinear ultrasound imaging of monodisperse microbubbles

Matalliotakis, Agisilaos; Waasdorp, Rick; Verweij, Martin D.; Maresca, David

**DOI**

[10.1103/PhysRevApplied.22.034062](https://doi.org/10.1103/PhysRevApplied.22.034062)

**Publication date**

2024

**Document Version**

Final published version

**Published in**

Physical Review Applied

**Citation (APA)**

Matalliotakis, A., Waasdorp, R., Verweij, M. D., & Maresca, D. (2024). Impact of wavefront shape on nonlinear ultrasound imaging of monodisperse microbubbles. *Physical Review Applied*, 22(3), Article 034062. <https://doi.org/10.1103/PhysRevApplied.22.034062>

**Important note**

To cite this publication, please use the final published version (if applicable). Please check the document version above.

**Copyright**

Other than for strictly personal use, it is not permitted to download, forward or distribute the text or part of it, without the consent of the author(s) and/or copyright holder(s), unless the work is under an open content license such as Creative Commons.

**Takedown policy**

Please contact us and provide details if you believe this document breaches copyrights. We will remove access to the work immediately and investigate your claim.

***Green Open Access added to TU Delft Institutional Repository***

***'You share, we take care!' - Taverne project***

**<https://www.openaccess.nl/en/you-share-we-take-care>**


Otherwise as indicated in the copyright section: the publisher is the copyright holder of this work and the author uses the Dutch legislation to make this work public.

## Impact of wavefront shape on nonlinear ultrasound imaging of monodisperse microbubbles

Agisilaos Matalliotakis,<sup>1</sup> Rick Waasdorp<sup>1</sup>,<sup>1</sup> Martin D. Verweij<sup>1,2</sup>,<sup>1,2</sup> and David Maresca<sup>1,\*</sup>

<sup>1</sup>*Department of Imaging Physics, Faculty of Applied Sciences, Delft University of Technology, 2628 CJ Delft, Netherlands*

<sup>2</sup>*Department of Biomedical Engineering, Erasmus University Medical Center, 3000 CA Rotterdam, Netherlands*

 (Received 5 March 2024; revised 10 July 2024; accepted 30 August 2024; published 26 September 2024)

The field of contrast-enhanced ultrasound (CEUS) combines nonlinearly oscillating microbubbles (MBs) with dedicated pulse sequences to reveal the vascular function of organs. Clinical ultrasound contrast agents consist of polydisperse MB suspensions with diameters ranging from 0.5 to 10  $\mu\text{m}$  and resonance frequencies ranging from 1 to 15 MHz. As a result, just a small fraction of MBs resonates at a given ultrasound frequency. MB suspensions with narrow size distributions can be tuned for a specific imaging frequency, boost CEUS sensitivity, and enable deeper vascular imaging. However, their enhanced nonlinear behavior makes imaging susceptible to nonlinear-wave-propagation artifacts. Here we numerically investigate the impact of the acoustic wavefront shape on the imaging of nonlinearly oscillating, monodisperse MBs. Specifically, our approach relies on an extension of the iterative nonlinear-contrast-source method that accounts for all nonlinear effects in CEUS. We demonstrate that supersonic X-shaped wavefronts referred to as “X waves” can be used to generate ultrasound images of monodisperse MBs without nonlinear-wave-propagation artifacts. In contrast, imaging based on focused, planar, and diverging wavefronts leads to significant nonlinear artifacts. Taken together, our results show that X waves can harness the full potential of monodisperse MBs by enabling their sensitive and specific detection in a tissue context.

DOI: [10.1103/PhysRevApplied.22.034062](https://doi.org/10.1103/PhysRevApplied.22.034062)

### I. INTRODUCTION

The combination of ultrasound imaging with intravenously administered echogenic microbubbles (MBs) has enabled significant advances, such as microvascular imaging beyond the diffraction limit [1]. MBs are nonlinear oscillators that scatter ultrasound efficiently thanks to their high contrast in density and compressibility with blood plasma [2] and their resonant behavior in the megahertz range [3]. Ultrasound pulse sequences [4] exploit nonlinear MB scattering to detect these vascular agents deep into tissues. A drawback of established pulse sequences such as amplitude-modulation (AM) is their susceptibility to cumulative nonlinear effects induced by wave propagation in MB suspensions [5,6]. Briefly, ultrasound waves propagating in a highly nonlinear effective medium such as a resonant MB suspension experience amplitude-dependent attenuation and amplitude-dependent speed-of-sound variations [7,8]. As a result, waves with different amplitudes are distorted differently through a MB suspension. In the end, waves carry that nonlinear distortion deeper into the medium, beyond the MB suspension, where they cause

echoes that make imaging based on amplitude modulation misclassify tissue as MBs.

In 2015, Renaud *et al.* [9] demonstrated that AM imaging based on the intersection of two diverging wavefronts could increase CEUS specificity. Maresca *et al.* [10] further optimized this approach into a sequence called “cross-amplitude-modulation” (xAM) that relies on cross-propagating plane waves intersecting with a constant angle. xAM has fundamental advantages over previous AM implementations. First, the constant cross-propagation angle ensures a constant reduction of cumulative nonlinear effects along the line where the wavefronts cross. Second, it generates a nondiffractive beam pattern with a constant beam width [11,12] that increases the lateral resolution of ultrasound images.

This study numerically investigates the specificity of imaging based on amplitude modulation for monodisperse MBs, the most nonlinear ultrasound contrast agent to date [13], for implementations using focused [4], planar [14], diverging [15], and X-shaped [10] ultrasonic wavefronts. We use the iterative nonlinear-contrast-source (INCS) method [16,17] to solve the full nonlinear acoustic wave equation in an acoustic medium containing a suspension of resonant monodisperse MBs. The INCS method was

\*Contact author: [d.maresca@tudelft.nl](mailto:d.maresca@tudelft.nl)

extended to account for ultrasound attenuation, medium inhomogeneities [18,19], local medium nonlinearities [20], and nonlinearities arising from the oscillatory behavior of resonant MBs surrounded by tissue-mimicking linear scatterers. [21] Together, these capabilities allow us to simulate CEUS-imaging modes such as AM and xAM.

This article is organized as follows. Sections II B and II A describe the INCS method and its application to imaging based on amplitude modulation. Section II C describes the media used in the simulations. Section II D describes the beam-forming process that was implemented to reconstruct ultrasound images. Section III A presents the incident and residual acoustic pressure fields generated by AM pulses in a homogeneous nonlinear medium free of ultrasound contrast agents. Section III B presents the total and residual acoustic pressure fields in a medium containing a monodisperse-MB suspension. Section III C describes the origin of nonlinear-wave-propagation artifacts observed in AM imaging. Section III D demonstrates the effect of the cross-propagation angle  $\theta$  on the suppression of the artifacts due to the nonlinear wave propagation. Section III E presents numerical AM images of monodisperse MBs generated with X-shaped, focused, planar, and diverging wavefronts. Finally, a brief analysis of the results generated is presented in Sec. IV, while concluding remarks of this study are given in Sec. V.

## II. METHODS

### A. Extension of the INCS method to account for nonlinear effects in CEUS

The linear incident pressure field resulting from an external source in a linear, lossless, homogeneous, and isotropic background medium can be mathematically described by the wave equation

$$c_0^{-2} \partial_t^2 p - \nabla^2 p = S_{\text{PR}}, \quad (1)$$

where  $p$  (in Pa) represents the acoustic pressure. The parameter  $c_0$  (in m/s) denotes the speed of sound in the background medium. The operator  $\nabla^2$  denotes the Laplacian and  $\partial_t^2$  represents the second-order time derivative. On the right-hand side of the equation, the primary-source term  $S_{\text{PR}}$  is used to describe the action of the transducer. The linear acoustic pressure distribution arising from the primary source in the background medium can be explicitly found as

$$p(\mathbf{x}, t) = G(\mathbf{x}, t) *_{\mathbf{x}, t} S_{\text{PR}}(\mathbf{x}, t), \quad (2)$$

where  $G(\mathbf{x}, t)$  is the Green's function of the background medium, and the operator  $*_{\mathbf{x}, t}$  denotes convolution over the spatiotemporal domain of  $S_{\text{PR}}$ . Because the background medium is simple,  $G(\mathbf{x}, t)$  is known analytically.

Realistic media are modeled by more-complex wave equations that also account for inhomogeneities, attenuation,

nonlinear behavior, etc. Within the doctrine of the INCS method, all terms in which the more-complex wave equation deviates from the simple-background wave equation in Eq. (1) are shifted to the right-hand side and are considered as contrast sources. The result is

$$c_0^{-2} \partial_t^2 p - \nabla^2 p = S_{\text{PR}} + S_{\text{CS}}(p), \quad (3)$$

where  $S_{\text{CS}}(p)$  is the total of all contrast-source terms that account for the inhomogeneity, attenuation, nonlinearity, and the like that are not exhibited by the background medium. The acoustic pressure distribution arising from the primary source in a realistic medium can be implicitly found as

$$p(\mathbf{x}, t) = G(\mathbf{x}, t) *_{\mathbf{x}, t} [S_{\text{PR}}(\mathbf{x}, t) + S_{\text{CS}}(p)]. \quad (4)$$

With the INCS method, an explicit solution is obtained in an iterative way—for example, by use of the Neumann iterative scheme

$$p^{(0)} = G(\mathbf{x}, t) *_{\mathbf{x}, t} S_{\text{PR}}(\mathbf{x}, t), \quad (5)$$

$$p^{(n)} = G(\mathbf{x}, t) *_{\mathbf{x}, t} [S_{\text{PR}}(\mathbf{x}, t) + S_{\text{CS}}(p^{(n-1)})] \\ = p^{(0)} + G(\mathbf{x}, t) *_{\mathbf{x}, t} S_{\text{CS}}(p^{(n-1)}) \quad (n \geq 1). \quad (6)$$

This general approach is used for the numerical simulations in this paper.

To simulate CEUS imaging, all nonlinear effects occurring during ultrasound wave propagation in a nonlinear medium containing nonlinearly scattering MBs must be taken into account. In addition, simulations should support scattering from tissue-mimicking linear scatterers that typically surround a MB suspension in biological tissues. On the basis of these criteria, the INCS equation was extended with extra contrast-source terms, resulting in the new nonlinear wave equation

$$c_0^{-2} \frac{\partial^2 p}{\partial t^2} - \nabla^2 p = S_{\text{PR}} + S_{\text{MB}}(p) + S_{\text{LS}}(p) \\ + S_{\text{global NL}}(p) + S_{\text{local NL}}(p), \quad (7)$$

where  $S_{\text{MB}}$  is the contrast-source term describing the scattering of the MBs in the suspension [21],  $S_{\text{LS}}$  is the contrast-source term describing the scattering of the linear scatterers in the linear-scatterer suspension [21], and  $S_{\text{global NL}}$  and  $S_{\text{local NL}}$  are the terms describing global [21] and local [20] medium nonlinearities, respectively. The sum of all the contrast-source terms yields the term  $S_{\text{CS}}(p)$  in Eq. (3), which is then convolved with the 4D spatiotemporal Green's function of the linear background medium to compute a nonlinear field correction. On the basis of the Neumann iterative scheme described in Eqs. (5) and (6), the INCS method successively generates an increasingly accurate solution of Eq. (7), taking into account nonlinear effects and multiple scattering.

### B. INCS implementation of AM pulse sequences

In this study, we simulate a 64-element ( $N_{tr} = 64$ ), 15 MHz linear transducer array emulating an L22-14vX probe (Verasonics, Kirkland, WA, USA). The transducer elements have height  $H_{el} = 1.4$  mm, width  $W_{el} = 0.08$  mm, and pitch  $P_{tr} = 0.1$  mm, and the total focal distance of the array  $z_{el}$ , which includes a lens in elevation, is 8 mm. The natural focus of the transducer array is  $(N_{tr} P_{tr})^2 / 4\lambda = 103$  mm in the azimuthal plane and  $H_{el}^2 / 4\lambda = 5$  mm in the elevational plane, with  $\lambda$  being the wavelength. All transmitted ultrasound waveforms used in this study are Gaussian-windowed sine bursts defined as follows:

$$s(t) = \exp\left[-\left(\frac{t - T_d}{T_w/2}\right)^2\right] \sin[2\pi f_0(t - T_d)], \quad (8)$$

where  $f_0 = 15$  MHz is the center frequency,  $T_w = 1.5/f_0 = 0.1$   $\mu$ s is the width of the Gaussian envelope, and  $T_d = 3/f_0 = 0.2$   $\mu$ s is the temporal delay of the window. The simulated medium is water, characterized by volumetric mass density  $\rho_0 = 1060$  kg/m<sup>3</sup> and speed of sound  $c_0 = 1482$  m/s.

The first AM sequence implemented in the INCS method is the sequence with X-shaped wavefronts [10].

xAM pulse transmissions proceed as follows: First, elements 1 to  $N/2$  and elements  $N/2 + 1$  to  $N$  of the array simultaneously transmit two axisymmetric, tilted plane waves with wavefronts that make angles  $\theta$  and  $-\theta$  with respect to the array [see pulse 1, Fig. 1(a)]. Second, only elements 1 to  $N/2$  transmit a single tilted plane wave at angle  $-\theta$  with respect to the array [see pulse 2, Fig. 1(a)]. Third, only elements  $N/2 + 1$  to  $N$  transmit a single symmetric plane wave at angle  $\theta$  with respect to the array [see pulse 3, Fig. 1(a)]. The two cross-propagating waves depicted as pulse 1 interfere in a small zone around a virtual bisector that separates the two half-apertures. Particles of the insonified medium that are positioned along the bisector experience an identical pressure amplitude from pulses 2 and 3, but a double pressure amplitude from pulse 1 (X-wave transmission). Note that the overpressure at the plane waves' intersection depicted in pulse 1 propagates along the bisector with a supersonic phase velocity

$$c_X = c_0 / \cos(\theta). \quad (9)$$

The second AM sequence implemented in the INCS method relies on focused ultrasound wavefronts as depicted in Fig. 1(b). Focused AM transmissions proceed

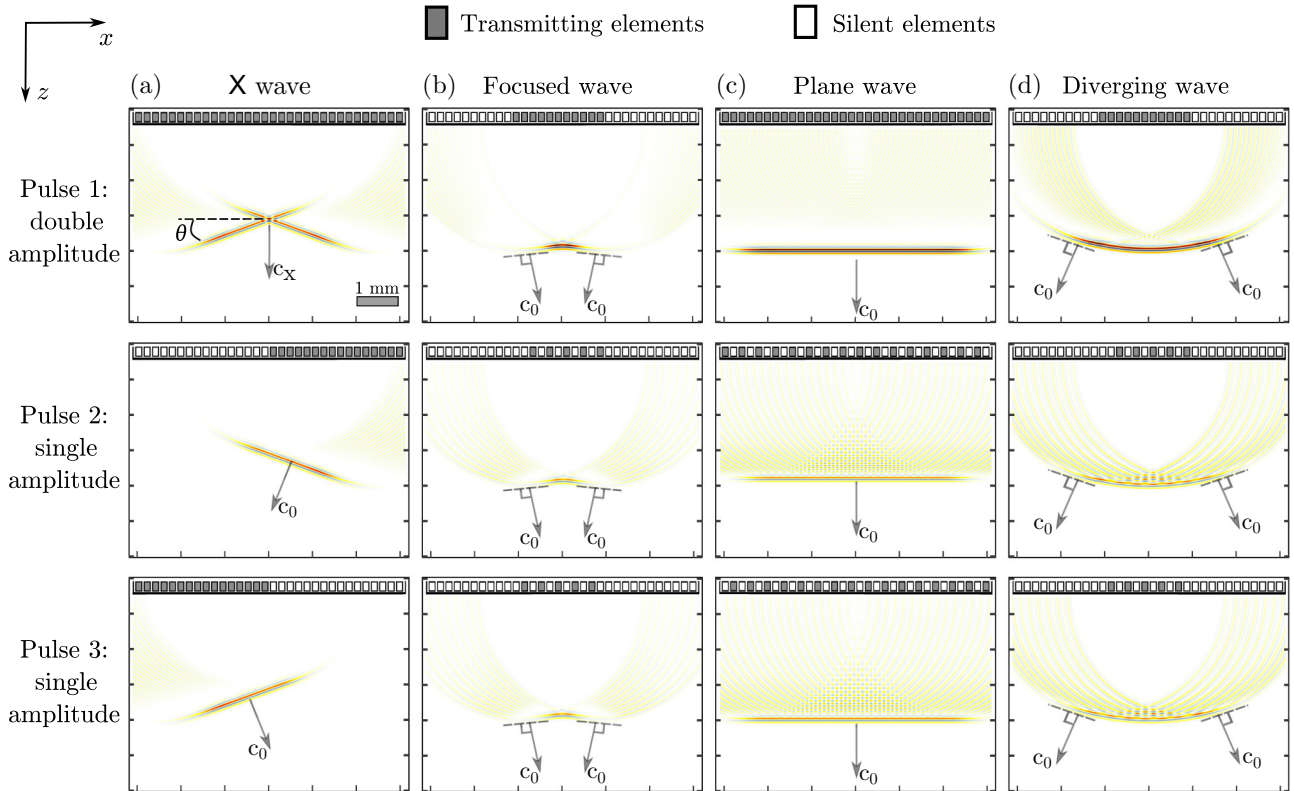


FIG. 1. Wavefront shapes belonging to the pulse sequences investigated for AM ultrasound imaging of monodisperse MBs. (a) xAM sequence with wavefront angle  $\theta = 20^\circ$ , (b) focused AM sequence, (c) plane wave AM sequence, and (d) diverging AM sequence. The first row shows the imaging pulses transmitted to elicit a double-amplitude response from the medium, while the second and third rows show the pulses transmitted to elicit a single-amplitude response from the medium. Arrows indicate wavefront velocities.

as follows: First, all elements of the array are activated following a parabolic delay law to generate a high-amplitude transmission [see pulse 1, Fig. 1(b)]. Second, even transducer elements of the same aperture are activated with use of the same delay law to generate a half-amplitude transmission [see pulse 2, Fig. 1(b)]. Third, odd transducer elements of the same aperture are activated with use of the same delay law to generate a second half-amplitude transmission [see pulse 3, Fig. 1(b)]. Here the focal distance  $z_f$  is set to 5 mm. Note that in focused AM, acoustic wavefronts propagate at speed of sound  $c_0$ .

The third AM sequence implemented in the INCS method relies on planar ultrasound wavefronts as seen in Fig. 1(c). Plane wave transmissions are generated by transmission of the same pulse with all elements of the transducer array. Here as well, the transmitted acoustic pressure amplitude is modulated with use of all, even, or odd elements of the array aperture [Fig. 1(c)]. Transmitted plane waves propagate at speed of sound  $c_0$  in the  $z$  direction.

The fourth AM sequence implemented in the INCS method relies on diverging acoustic wavefront transmissions. A virtual point source located at  $(x_f, z_f) = (0, -3)$  mm is used to generate the diverging delay law. Here as well, the transmitted acoustic pressure amplitude is modulated with use of all, even, or odd elements of the array aperture [Fig. 1(d)]. Transmitted diverging waves also propagate at speed of sound  $c_0$ .

### C. Simulation of a monodisperse-MB suspension

The dimensions of the computational domain are set to  $X \times Y \times Z = 6.4 \times 1.5 \times 10$  mm<sup>3</sup> as illustrated in Fig. 2. To accurately solve the full nonlinear wave equation up to the second-harmonic frequency ( $h = 2$ ), we choose a Nyquist frequency  $F_{Nyq}$  equal to at least  $h + 1.5 = 3.5$  times the center ultrasound frequency. This corresponds to a sampling frequency  $F_s$  of  $2F_{Nyq} = 2 \times 3.5 \times 15 = 105$  MHz as a basis for discretizing the spatiotemporal domain. Furthermore, it is known that we need at least  $j = h + 1 = 3$  iterations for an accurate prediction of the second harmonic [17]. To achieve a relative root-mean-square error of  $10^{-6}$  between successive iterations below, we take  $j = 5$  iterations. Consequently, our simulations account for MB interactions up to fourth-order multiple scattering [21].

We consider a monodisperse-MB suspension confined in a cylindrical volume positioned at the center of the simulation domain  $(x, y, z) = (0, 0, 5)$  mm, with a radius of 1 mm in the  $x$ - $z$  plane and a length of 1.4 mm for the  $y$  dimension, as shown in Fig. 2(a). This geometry is chosen to mimic MBs filling the lumen of a blood vessel. A MB radius  $R$  of  $0.6$   $\mu$ m, corresponding to a resonance frequency of 15 MHz in the elastic oscillation regime, is selected to match the center frequency of the simulated transducer array. We use the Marmottant model [3] to

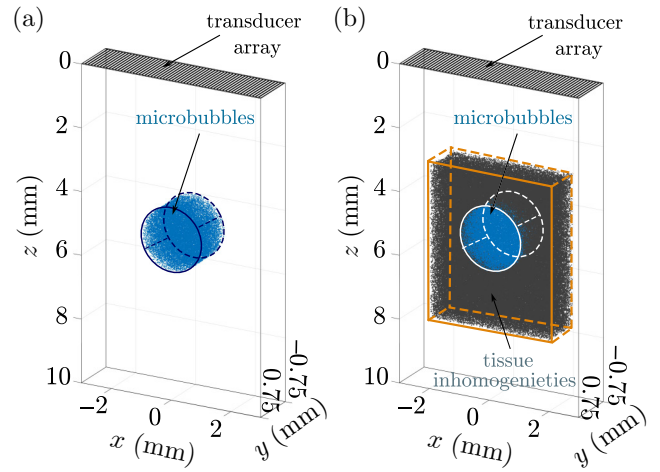


FIG. 2. Media simulated in the INCS method. (a) Computational domain containing a monodisperse-MB concentration of  $5.7 \times 10^6$  ml<sup>-1</sup> (blue) of  $0.6$   $\mu$ m radius bubbles, embedded in water. (b) Configuration incorporating a tissue-mimicking-scatterer concentration of  $6.2 \times 10^6$  ml<sup>-1</sup> (gray) surrounding the monodisperse-MB suspension in (a).

emulate the nonlinear behavior of each MB in the simulation domain. Simulated material properties of MBs are provided in Table I [22].

A total of 25 000 monodisperse MBs are randomly distributed within the cylindrical volume, resulting in a MB concentration of  $5.7 \times 10^6$  ml<sup>-1</sup> and a gas volume concentration of  $5.15 \times 10^{-6}$ , which follows injection protocols reported by MB manufacturers (e.g., Fujifilm VisualSonics, Toronto, ON, Canada).

To reveal AM-imaging artifacts due to nonlinear wave propagation, we also consider a second domain with tissue-mimicking linear scatterers [Fig. 2(b)]. These are located in a volume of  $L \times W \times H = 4 \times 1.5 \times 5$  mm<sup>3</sup> surrounding the MB suspension. The linear scatterers have a spherical radius of  $0.6$   $\mu$ m to match the speckle pattern generated by monodisperse MBs. Their concentration is  $6.2 \times 10^6$  ml<sup>-1</sup>, and their volume concentration is  $5.61 \times 10^{-6}$ , which is approximately similar to that of the MB suspension. The scattering coefficient  $g$  of the linear scatterers [21] is set to  $6.57 \times 10^{-6}$  m to match the scattering level of monodisperse MBs.

TABLE I. Material properties of a single simulated MB with  $R = 0.6$   $\mu$ m.  $\kappa_s$  is the shell viscosity,  $\sigma_w$  is the surface tension of water,  $\sigma_R$  is the effective surface tension,  $\gamma$  is the polytropic exponent of the gas encapsulated in the bubble,  $\chi$  is the shell elasticity, and  $\mu$  is the gas core viscosity.

$\kappa_s$ (kg/s)	$\sigma_w$ (N/m)	$\sigma_R$ (N/m)	$\gamma$	$\chi$ (N/m)	$\mu$ (Pa s)
$2.4 \times 10^{-9}$	0.072	0.01	1.07	0.5	$2 \times 10^{-3}$

### D. Ultrasound image reconstruction

xAM and focused AM images are reconstructed line-by-line with the use of 42 sliding subapertures across the MB suspension. For each subaperture position, three pulses are transmitted sequentially as illustrated in Figs. 1(a) and 1(b), leading to a total of 126 ultrasound transmissions per AM image. To acquire radiofrequency data corresponding to each image line, instead of moving the transducer, we translate the position of the MB suspension laterally with steps  $dx = 0.1$  mm, which is the pitch of the imaging array. The reconstructed-image width  $x$  ranges from  $-2.1$  to  $2.1$  mm. Plane wave and diverging wave AM images are reconstructed from three pulse transmissions only, as each insonification captures a wide 2D field of view [Figs. 1(c) and 1(d)]. B-mode images are reconstructed with the use of the first pulse of each AM sequence.

xAM image reconstruction is performed along the bisector as illustrated in Fig. 3. The transmit distance  $d_{TX}$  and the transmit time of flight  $\tau_{TX}$  to a scatterer  $\mathbf{X}_s = (x_s, z_s)$  are given by

$$d_{TX}(\theta, z_s) = D_h \tan(\theta) + z_s, \quad (10)$$

$$\tau_{TX} = \frac{d_{TX}}{c_X}, \quad (11)$$

with  $D_h = N_{tr}P_{tr}/2$  being the length of the half aperture. The receive distance  $d_{RX}$  and receive time of flight  $\tau_{RX}$  are given by

$$d_{RX}(\mathbf{X}_s) = \sqrt{(x_s - x_i)^2 + z_s^2}, \quad (12)$$

$$\tau_{RX} = \frac{d_{RX}}{c_0}, \quad (13)$$

with  $x_i$  the position of the  $i$ th element. Knowledge of transmit and receive time of flights enables the reconstruction of one image line with the use of a conventional delay-and-sum beam-forming algorithm [23]. By repetition of the process for each transmitting subaperture position, a xAM image of the MB suspension is generated.

Focused AM image reconstruction is performed line-by-line as well with the use of usual transmit and receive times of flight. For plane wave and diverging wave image reconstruction, we use the MATLAB Ultrasound Toolbox (MUST) [24] and a virtual-point-source formulation as described by Perrot *et al.* [23].

## III. RESULTS

### A. Acoustic pressure fields in the absence of MBs

To isolate nonlinear effects due to wave propagation, we first solve the full nonlinear wave equation in a homogeneous nonlinear medium consisting of water that is free of MBs.

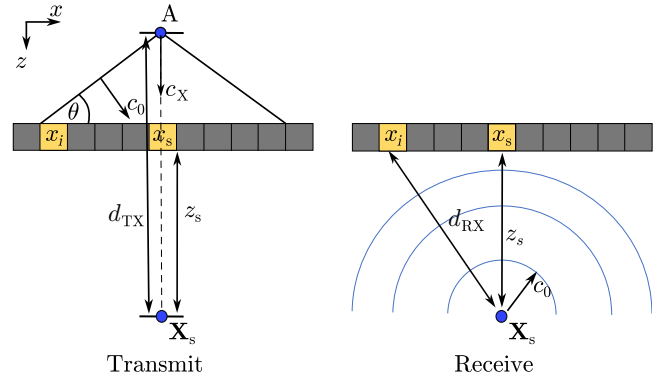


FIG. 3. Transmit and receive geometry model used for xAM image reconstruction.

Figure 4 presents the simulated incident pressure fields generated by the first pulse of each AM sequence, as well as the time delays and apodization functions used to generate these beam patterns. To ensure a fair comparison of nonlinear effects, we equated the average acoustic pressure delivered by the first pulse of each sequence on the  $z$  axis between  $z = 4$  mm and  $z = 6$  mm (see Appendix A).

We report in Fig. 4(a) the X-wave beam pattern simulated for angle  $\theta = 20^\circ$ . All 64 elements are used in transmission, and a Tukey window apodization, with parameter  $\alpha = 0.3$  representing the ratio of the cosine-tapered section length to the entire window length, is applied along the elements of each half aperture of the array to mitigate the side-lobe level and diffraction effects. The nondiffractive X-wave beam pattern exhibits a constant beam width along the bisector. Beyond the X-wave intersection zone, a noticeable acoustic pressure drop is observed along the bisector.

Figure 4(b) displays the focused-wave beam pattern generated with parabolic time delays applied to a subaperture of 22 elements apodized with a Tukey window ( $\alpha = 0.3$ ). The beam focus  $z$  is equal to 4.75 mm, corresponding to an  $f$  number of 2.27. Most of the focused beam energy is concentrated between  $z = 4$  mm and  $z = 6$  mm. The focal length is shorter than that of the X-wave beam, whereas in the lateral direction, the focused beam is noticeably wider than the X-wave beam.

Figure 4(c) displays the plane-wave beam pattern generated with all 64 elements apodized with a Tukey window ( $\alpha = 0.3$ ). The plane-wave beam focus  $z$  is 5.25 mm, and the elevated amplitude around  $z = 5$  mm is due to the focusing in elevation.

Figure 4(d) displays the diverging beam pattern generated by inversion of the time delays used in Fig. 4(b). Here the total beam focus  $z$  is equal to 4.65 mm, also due to the focusing in elevation.

The primary objective of CEUS imaging is to suppress nonlinear effects arising from wave propagation in the medium of interest, while retaining nonlinear effects

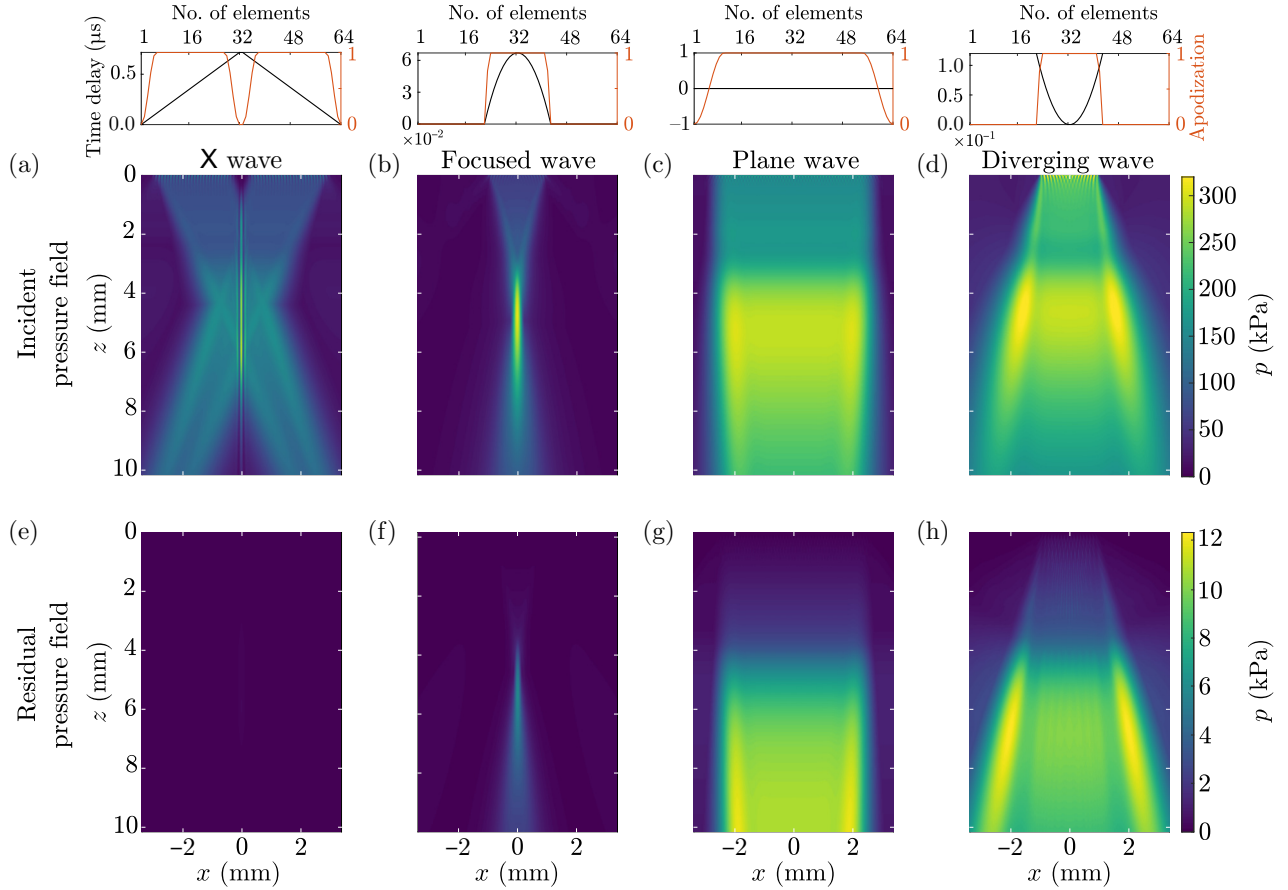


FIG. 4. Acoustic pressure fields in a homogeneous nonlinear medium consisting of water. Top row: Time delays (black) and apodization functions (orange) used for the first pulse transmissions. (a)–(d) Incident pressure fields generated by the first pulse transmission of each sequence with X-shaped, focused, planar, and diverging beams, respectively. (e)–(h) Residual AM pressure fields for the xAM, focused AM, planar AM, and diverging AM pulse sequences, respectively. xAM transmissions are simulated for  $\theta = 20^\circ$ .

arising from ultrasound contrast agents administered in that medium. To investigate the ability of AM sequences based on X-shaped, focused, planar, and diverging wavefronts to suppress nonlinear-wave-propagation effects, we report the residual acoustic pressure fields after the AM operation (pulse 1 – pulse 2 – pulse 3) and display them in Figs. 4(e)–4(h).

We observe that AM pulse sequences based on focused, planar, and diverging wavefronts suffer from effects arising from nonlinear wave propagation and local noncollinear nonlinear interactions [20], even in the absence of MBs. The residual xAM pressure field, in contrast, is nearly free of nonlinear effects. Quantitatively, the residual xAM pressure field exhibits the lowest amplitude, with a peak of 0.26 kPa [see Fig. 10(a) in Appendix B], followed by the residual focused AM pressure field with a peak of 6 kPa, the residual plane-wave AM pressure field with a peak of 11.9 kPa, and the residual diverging AM pressure field with a peak of 12.3 kPa.

Qualitatively, for the xAM case [Fig. 10(a)], the highest residual pressure values are observed along the bisector. However, we observe that below the plane wave

intersection zone, the residual xAM pressure level drops significantly.

For the focused AM case [Fig. 4(f)], nonlinearities peak at the focus but extend beyond the focus because of cumulative nonlinear wave propagation effects, following the shape of the transmitted beam [Fig. 4(b)].

For the plane-wave AM case [Fig. 4(g)] a gradual onset of nonlinearities is observed as expected for cumulative nonlinear effects due to wave propagation [25]. Additionally, a higher amplitude is observed on the sides of the plane-wave beam due to the larger incident pressure in those regions.

For the diverging AM case [Fig. 4(h)], the behavior is similar to that in the plane-wave case, and nonlinearities reach the highest peak amplitude in comparison with all the other cases.

## B. Acoustic pressure fields in the presence of monodisperse MBs

Total acoustic pressure fields generated by the first pulse of each AM sequence in the presence of a



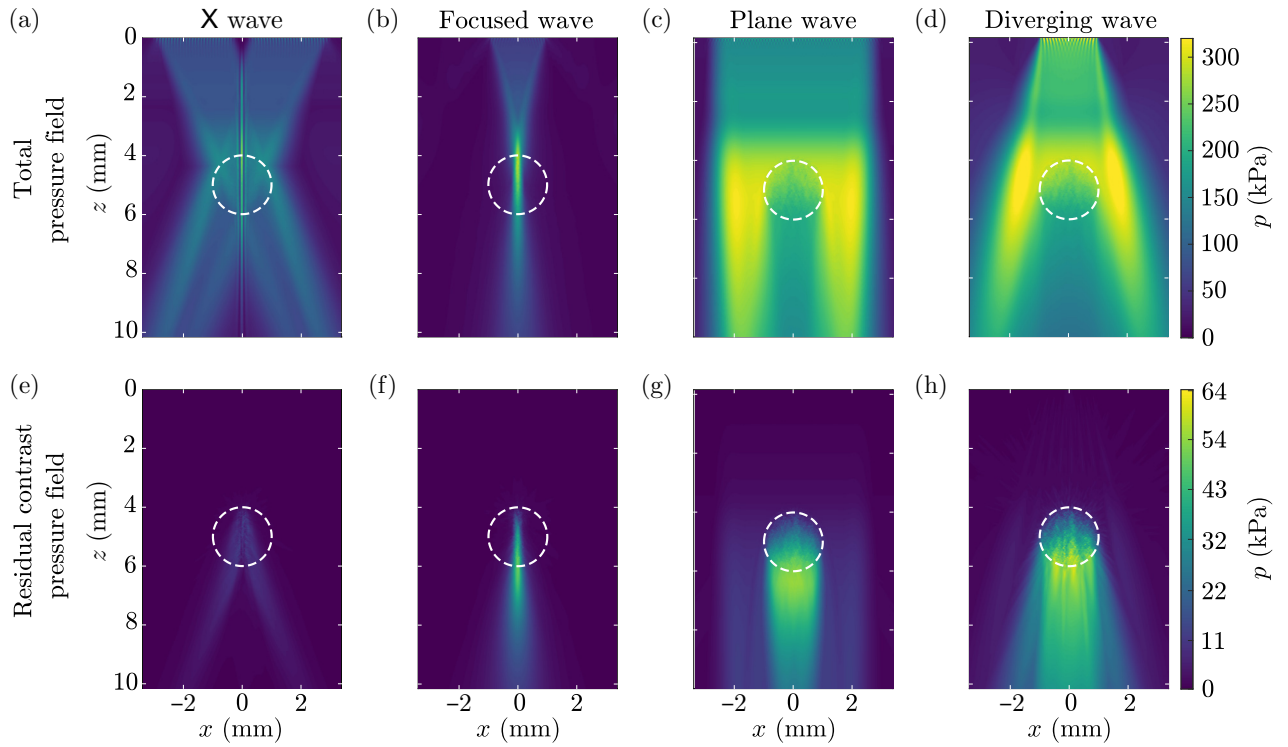


FIG. 5. Acoustic pressure fields in the presence of resonant monodisperse MBs. (a)–(d) Total acoustic pressure fields generated by the first pulse transmission of each sequence with X-shaped, focused, planar, and diverging beams, respectively. (e)–(h) Residual acoustic pressure fields generated by the xAM, focused AM, planar AM, and diverging AM pulse sequences, respectively.

resonant monodisperse MB suspension are displayed in Figs. 5(a)–5(d). The X-wave pressure field [Fig. 5(a)] is attenuated below the MB suspension and shows a peak acoustic pressure at  $(x, z) = (0, 7)$  mm of 166 kPa, compared with 216 kPa in water without MBs [Fig. 4(a)]. Compared with the X-wave case, the focused pressure field shows a more-substantial level of attenuation below of the MB suspension, with peak acoustic pressure at  $(x, z) = (0, 7)$  mm of 140 kPa, compared with 205 kPa in water without MBs [Fig. 4(b)]. Similarly, the planar pressure field shows a peak pressure of 186 kPa, compared with 272 kPa in water without MBs [Fig. 4(c)], and the diverging pressure field shows a peak pressure of 168 kPa, compared with 243 kPa in water without MBs [Fig. 4(d)].

Residual AM pressure fields in the presence of a suspension of resonant monodisperse MBs are reported in Figs. 5(e)–5(h). For the xAM case, a better view of the spatial pattern of Fig. 5(e) is illustrated in Fig. 10(b) in Appendix B. We observe that nonlinear effects accumulate along the direction of propagation of each plane wave. However, along the bisector and below the MB suspension, nonlinear effects are suppressed. The residual xAM pressure field reaches a maximum of 15.2 kPa within the MB suspension, as desired for a CEUS pulse sequence,

and immediately drops beyond the MB suspension. A peak pressure of 1.7 kPa is measured at  $z = 6.3$  mm.

For the focused AM case [Fig. 5(f)], the amplitude of the residual pressure field builds up inside the MB suspension along the  $z$  axis and reaches a maximum of 51 kPa at  $z = 5.7$  mm, which is deeper than the transducer focus of 5.25 mm. Below the MB suspension, the amplitude of the residual AM pressure field remains high and reaches 47.7 kPa at  $z = 6.3$  mm, which is 28 times higher than for the xAM case.

For the planar AM case [Fig. 5(g)], the amplitude of the residual pressure field builds up along the  $z$  axis and expands across the width of the plane-wave beam profile. We observe an increase of nonlinear effects within and below the MB suspension, which is as wide as the MB cloud. Cumulative nonlinear effects are also observed outside the lateral extension of the MB suspension, i.e. for  $x < -1$  mm and  $x > 1$  mm; these are caused by nonlinear wave propagation alone. The planar AM pressure field reaches a peak of 52 kPa within the MB suspension and 53.4 kPa at  $z = 6.3$  mm, which is 31 times higher than for the xAM case.

For the diverging AM case [Fig. 5(h)], we observe an increase of nonlinear effects below the MB suspension that spans the full width of the MB suspension as well. The AM

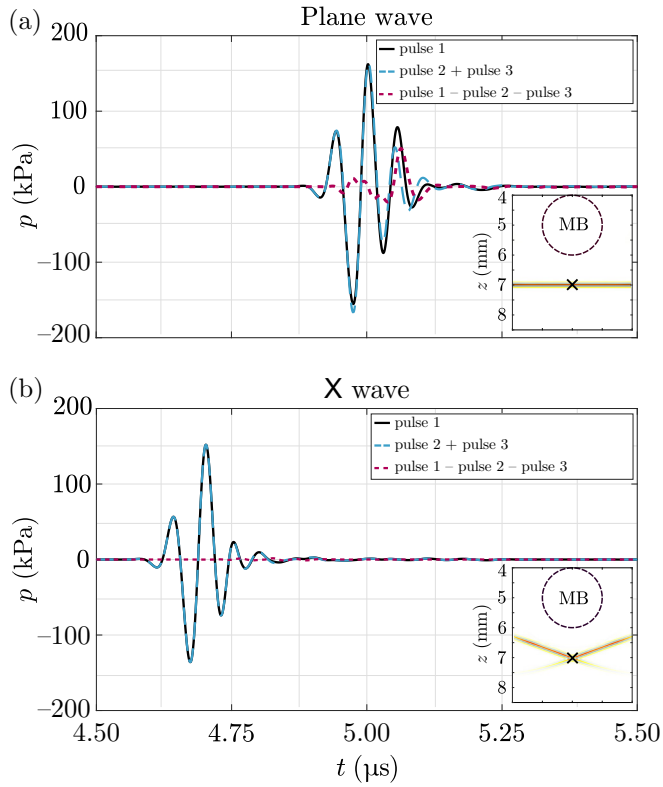


FIG. 6. Pulses at a depth of 7 mm. (a) Waveforms for the planar AM pulse sequence. (b) Waveforms for the xAM pulse sequence.

pressure field peaks at 58.6 kPa within the MB suspension and at 59.4 kPa at  $z = 6.3$  mm, which is 35 times higher than for the xAM case.

### C. Reason for reduction of nonlinear wave propagation artifacts by an X-shaped wavefront

To elucidate why cumulative nonlinear effects do not build up along the bisector in the xAM case, in Fig. 6 we present the transmitted waveforms with a planar wavefront and an X-shaped wavefront at depth  $z = 7$  mm, which is below the MB suspension.

Figure 6(a) displays the three pulses of the planar AM sequence at a depth of 7 mm. The pulses reach  $z = 7$  mm in  $4.73 \mu\text{s}$  (including a delay of  $0.1 \mu\text{s}$ ), corresponding to a wave velocity of 1482 m/s. The residual waveform derived from the AM operation exhibits a nonzero pressure amplitude with a residual AM peak pressure of 50.6 kPa, compared with 162.2 kPa for the first pulse of the sequence. We observe that the sum of the second and third pulses of the sequence [Fig. 6(a), dashed magenta line] does not match the waveform of double-amplitude pulse 1 [Fig. 6(a), continuous black line].

In comparison in Fig. 6(b) shows that the three pulses of the xAM sequence propagate to a depth of 7 mm in  $4.45 \mu\text{s}$  (including a delay of  $0.1 \mu\text{s}$ ), corresponding to

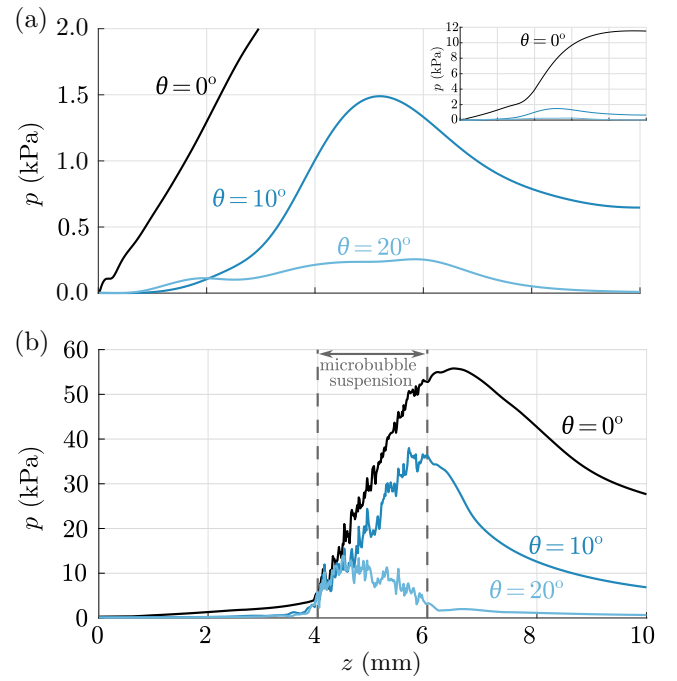


FIG. 7. xAM peak residual pressure along the bisector, as a function of depth for increasing angle  $\theta$ . (a) Residual pressure profiles in the absence of MBs. (b) Residual pressure profiles in the presence of monodisperse MBs. The boundaries of the MB suspension are indicated with dashed vertical lines.

a supersonic wave velocity  $c_x$  of 1577 m/s. The sum of the second and third pulses of the xAM sequence overlaps nearly perfectly with the first pulse. The residual waveform derived from the xAM operation exhibits a quasizero residual pressure amplitude of 1.7 kPa after the xAM operation, compared with 152.1 kPa for the first pulse.

### D. Effect of the cross-propagation angle $\theta$ on the reduction of nonlinear artifacts

Figures 7(a) and 7(b) display the peak of the AM residual pressure as a function of depth along the bisector, in the absence and in the presence of monodisperse MBs, respectively. Figure 7(a) shows that higher angles  $\theta$  are more effective at suppressing effects arising from nonlinear wave propagation in the medium.

Figure 7(b) shows that the presence of monodisperse MBs leads to a substantial increase in the residual xAM peak pressure level within the boundaries of the MB suspension, as desired for a CEUS imaging mode. However, we observe that angles  $\theta$  of  $0^\circ$  and  $10^\circ$  do not strongly suppress nonlinear effects below the MB suspension. In contrast, an angle  $\theta$  of  $20^\circ$  strongly reduces the xAM pressure amplitude beyond the boundary of the MB suspension.

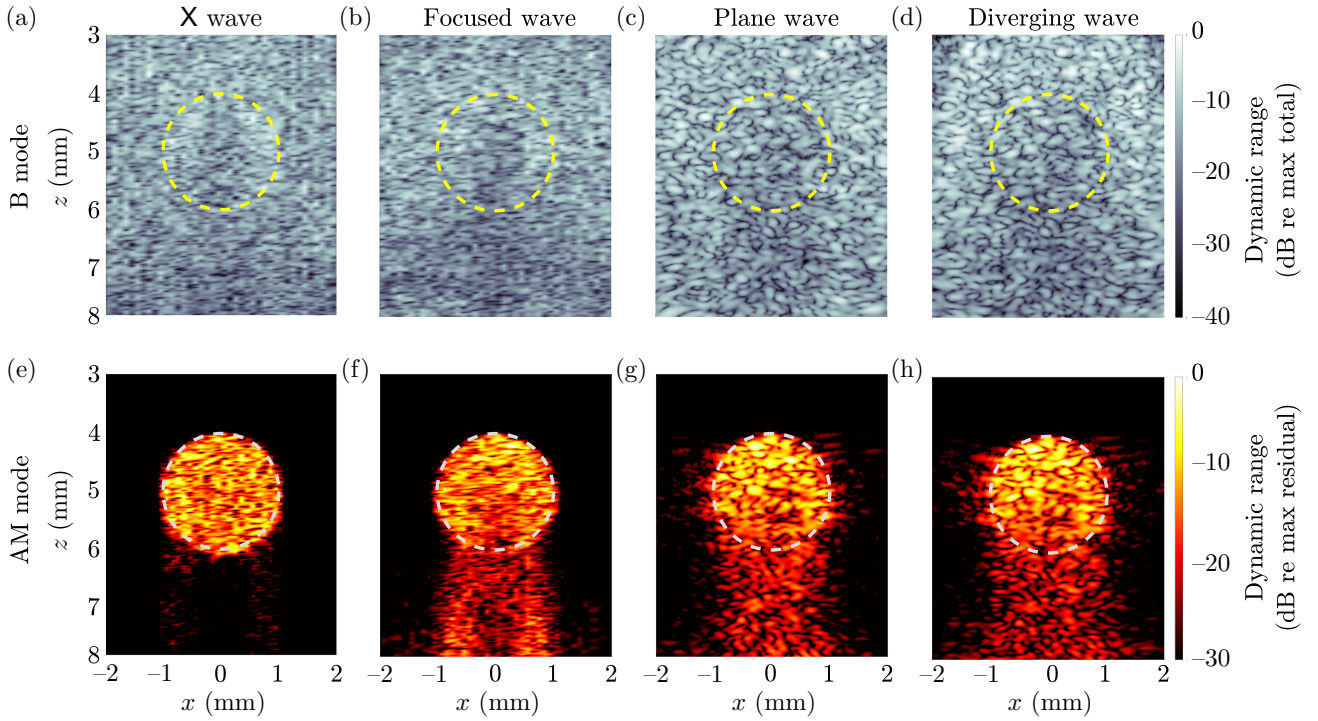


FIG. 8. Numerical B-mode and AM ultrasound images of monodisperse MBs. (a)–(d) Single-shot ultrasound images acquired with X-shaped, focused, planar, and diverging wavefronts, respectively. (e)–(h) AM ultrasound images acquired with X-shaped, focused, planar, and diverging wavefronts, respectively. The position of the MB suspension is outlined by a dashed circle. The surrounding domain is filled with tissue-mimicking linear scatterers.

### E. Impact of wavefront shape on AM imaging of monodisperse MBs

In this section, we report the use of the INCS method to simulate ultrasound imaging of a monodisperse MB suspension by applying AM pulse sequences with four different wavefront shapes (Fig. 1). The computational domain is shown in Fig. 2(b). Conventional single-shot ultrasound images, also referred to as “B mode images,” are reported in Figs. 8(a)–8(d). The backscattered amplitude arising from tissue-mimicking linear scatterers and resonant monodisperse MBs generates a similar echogenicity level, independent of the acoustic wavefront shape. As such, B mode images do not allow us to disentangle monodisperse MBs and tissue-mimicking scatterers.

AM images generated with each wavefront shape are reported in Figs. 8(e)–8(h). The xAM sequence [Fig. 8(e)] generates a highly specific image of monodisperse MBs. In contrast, AM sequences based on focused, planar, and diverging wavefronts [Figs. 8(f)–8(h)] generate images of MBs that suffer from significant nonlinear wave propagation artifacts below the MB suspension. The level of nonlinear artifacts is  $-30$  dB for the xAM image,  $-9$  dB for the focused AM image,  $-12$  dB for the plane-wave AM image, and  $-12$  dB for the diverging AM image.

### IV. DISCUSSION

We report a numerical investigation of CEUS imaging and demonstrate that AM imaging based on X-shaped wavefronts enables specific and sensitive imaging of monodisperse MBs at a high ultrasound frequency. Our results reveal that the shape of transmitted ultrasonic wavefronts plays a critical role in the specificity of AM ultrasound imaging of monodisperse MBs. Widely used AM pulse sequence implementations based on focused, planar, and diverging wavefronts [Figs. 1(b)–1(d)] are all subject to significant nonlinear wave propagation artifacts appearing below monodisperse MB suspensions [Figs. 8(f)–8(h)].

The INCS method enables us to disentangle different nonlinear effects involved in CEUS. In the absence of MBs, a first observation is that AM pulse sequences for all four wavefront shapes capture cumulative nonlinear effects caused by ultrasound wave propagation, despite the low acoustic pressure transmitted in the medium, which corresponds to a mechanical index of 0.074 in our study [Figs. 4(f)–4(h)]. A second observation is that a resonant monodisperse MB suspension amplifies cumulative nonlinear wave propagation effects in the direction of wave propagation for all wavefront shapes investigated [Figs. 5(e)–5(h)]. As a result, for the focused, planar, and diverging wavefronts, the AM operation is compromised below the monodisperse MB suspension as the pulses

involved do not cancel each other anymore [Fig. 6(a)]. This amplitude dependent nonlinear scattering effect leads to nonlinear wave propagation artifacts in AM images of monodisperse MBs [Figs. 8(f)–8(h)].

X-shaped wavefronts provide a solution to this problem. In the absence of MBs, residual xAM pressure fields prevent cumulative nonlinear wave propagation effects along the bisector, i.e., the imaging line, as seen in Fig. 4(e). In the presence of monodisperse MBs, cumulative nonlinear effects are visible in the direction of propagation of each cross-propagating plane wave [see Fig. 10(b) in Appendix B]; however, nonlinear effects do not build up along the bisector. In xAM imaging, the segments of each wavefront that contribute to the double amplitude can copropagate only for short periods of time. As a consequence, amplitude dependent cumulative nonlinear effects are minimized and higher angles  $\theta$  lead to higher suppression of these effects (Fig. 7).

A limitation of our study is that we investigate AM ultrasound imaging of a perfectly monodisperse ultrasound contrast agent rather than an ultrasound contrast agent with a narrow size distribution. However, nonlinear artifacts observed in our study are therefore maximized, and our study represents the worst-case test scenario for xAM imaging. Another limitation is that we investigate only perfectly symmetric geometries. In the future, it would be interesting to evaluate the effect of a scattering structure located in the path of one of the two cross-propagating plane waves. Nevertheless, *in vivo* experiments prove that xAM imaging also performs well in nonsymmetric soft biological tissue [26]. Another interesting pulse sequence to investigate would be a pulse-inversion sequence. It is acknowledged that pulse inversion sequences are prone to artifacts [5] since they were initially developed to isolate the second harmonic generated by nonlinear wave propagation [27,28].

Our study also has implications for the field of ultrasound localization microscopy [29]. Approaches that rely on AM sequences with focused, planar, or diverging wavefronts [15] are likely to be subject to artifacts, especially when one is mapping the coronary vasculature of the inferior myocardial wall, which sits below the left ventricle chamber filled with MBs.

## V. CONCLUSIONS

We numerically investigated AM ultrasound imaging of monodisperse MBs for implementations relying on X-shaped, focused, planar, and diverging acoustic wavefronts. We show that xAM ultrasound imaging can detect monodisperse MBs, the most nonlinear ultrasound contrast agent to date, with high sensitivity and specificity. All other AM sequence implementations were prone to nonlinear wave propagation artifacts. This study paves the way

for numerical investigations and optimization of CEUS imaging.

## ACKNOWLEDGMENTS

This research was supported by the project ‘‘Optoacoustic sensor and ultrasonic microbubbles for dosimetry in proton therapy’’ of the Dutch National Research Agenda, which is partly financed by the Dutch Research Council (NWO). R.W. was supported by a grant from the Medical Delta Ultrafast Ultrasound Heart and Brain Program. We thank G. Renaud and B. Heiles for fruitful discussions.

## APPENDIX A: EQUALIZATION OF INCIDENT ACOUSTIC PRESSURE LEVELS

In this paper we compare AM sequences for four different wavefront shapes. These are obtained with differing numbers of active elements, different time delays, and apodization, which may result in substantial differences in the incident pressure fields generated. To ensure a fair comparison of CEUS imaging results, it is necessary to deliver the same average peak pressure within the MB suspension for all cases. Furthermore, since image reconstruction for the X-wave and focused-wave methods is performed in a line-by-line format, it is critical to equalize the average peak pressure along the bisector at the location of the MB suspension ( $x = 0$  mm,  $4$  mm  $< z < 6$  mm). We chose to deliver an average peak acoustic pressure of 285.5 kPa over this interval for the first pulse of each AM pulse sequence. This corresponds to a mechanical index of 0.074. The resulting peak pressure as a function of depth along the bisector is given in Fig. 9 for each AM pulse sequence.

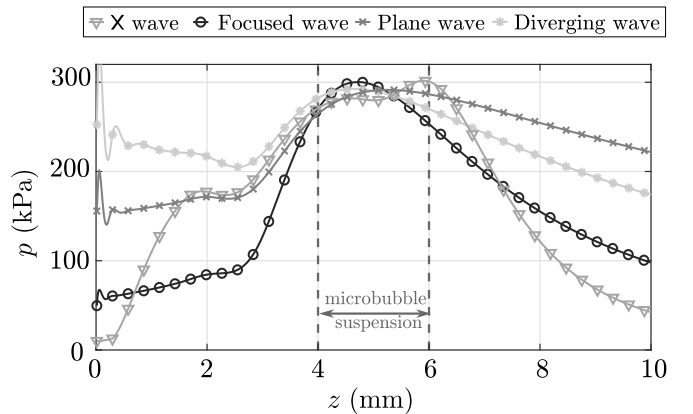


FIG. 9. Equalization of the average acoustic pressure transmitted by the first pulse of each sequence. Transmission for (a) X wave (triangles), (b) focused wave (circles), (c) plane wave (crosses), and (d) diverging wave (asterisks). The position of the MB suspension is indicated by the dashed vertical lines.

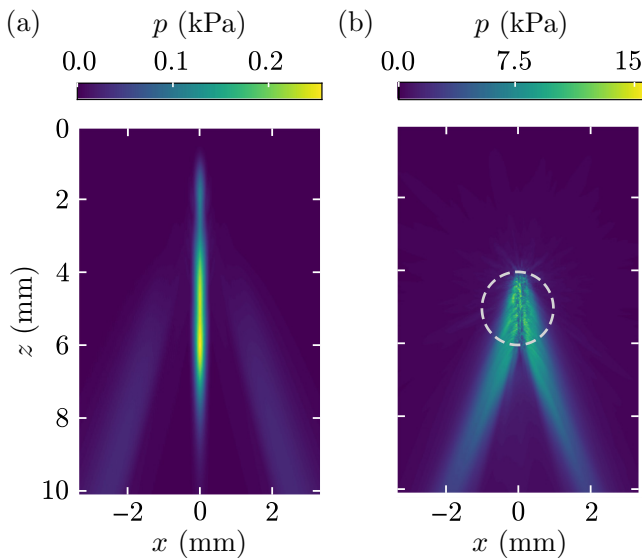


FIG. 10. Residual xAM pressure fields in (a) a homogeneous nonlinear medium consisting of water without MBs and (b) a medium consisting of water with nonlinearly oscillating monodisperse MBs. Dashed white lines indicate the position of the MB suspension.

### APPENDIX B: RESIDUAL XAM PRESSURE FIELDS IN THE ABSENCE AND IN THE PRESENCE OF MONODISPERSE MICROBUBBLES

To better visualize the residual xAM pressure fields reported in Figs. 4(e) and 5(e), in Fig. 10 we show the same results using a smaller pressure range.

[1] C. Errico, J. Pierre, S. Pezet, Y. Desailly, Z. Lenkei, O. Couture, and M. Tanter, Ultrafast ultrasound localization microscopy for deep super-resolution vascular imaging, *Nature* **527**, 499 (2015).

[2] B. Heiles, D. Terwiel, and D. Maresca, The Advent of Biomolecular Ultrasound Imaging, *Neuroscience* **474**, 122 (2021).

[3] P. Marmottant, S. van der Meer, M. Emmer, M. Versluis, N. de Jong, S. Hilgenfeldt, and D. Lohse, A model for large amplitude oscillations of coated bubbles accounting for buckling and rupture, *J. Acoust. Soc. Am.* **118**, 3499 (2005).

[4] M. Averkiou, M. Bruce, J. Powers, P. Sheeran, and P. Burns, Imaging methods for ultrasound contrast agents, *Ultrasound Med. Biol.* **46**, 498 (2020).

[5] M.-X. Tang and R. Eckersley, Nonlinear propagation of ultrasound through microbubble contrast agents and implications for imaging, *IEEE Trans. Ultrason. Ferroelectr. Freq. Control* **53**, 2406 (2006).

[6] G. ten Kate, G. Renaud, A. Akkus, S. van den Oord, F. ten Cate, V. Shamdasani, R. Entekin, E. Sijbrands, N. de Jong, J. Bosch, A. Schinkel, and A. F. van der Steen, Far-wall

pseudoenhancement during contrast-enhanced ultrasound of the carotid arteries: Clinical description and in vitro reproduction, *Ultrasound Med. Biol.* **38**, 593-600 (2012).

[7] M. Emmer, H. J. Vos, D. E. Goertz, A. van Wamel, M. Versluis, and N. de Jong, Pressure-dependent attenuation and scattering of phospholipid-coated microbubbles at low acoustic pressures, *Ultrasound Med. Biol.* **35**, 102 (2009).

[8] A. J. Sojahrood, Q. Li, H. Haghi, R. Karshafian, T. M. Porter, and M. C. Kolios, Probing the pressure dependence of sound speed and attenuation in bubbly media: Experimental observations, a theoretical model and numerical calculations, *Ultrason. Sonoch.* **95**, 106319 (2023).

[9] G. Renaud, J. Bosch, A. F. van der Steen, and N. de Jong, Increasing specificity of contrast-enhanced ultrasound imaging using the interaction of quasi counter-propagating wavefronts: A proof of concept, *IEEE Trans. Ultrason. Ferroelectr. Freq. Control* **62**, 1768 (2015).

[10] D. Maresca, D. P. Sawyer, G. Renaud, A. Lee-Gosselin, and M. G. Shapiro, Nonlinear X-wave ultrasound imaging of acoustic biomolecules, *Phys. Rev. X* **8**, 041002 (2018).

[11] S. Nagai and K. Iizuka, A practical ultrasound axicon for non-destructive testing, *Ultrasonics* **20**, 265 (1982).

[12] T. L. Szabo, *Diagnostic Ultrasound Imaging: Inside Out* (Academic Press, San Diego, 2014).

[13] T. Segers, P. Kruizinga, M. Kok, G. Lajoine, N. de jong, and M. Versluis, Monodisperse versus polydisperse ultrasound contrast agents: Non-linear response, sensitivity, and deep tissue imaging potential, *Ultrasound Med. Biol.* **44**, 1482 (2018).

[14] C. Tremblay-Darveau, R. Williams, L. Milot, M. Bruce, and P. Burns, Visualizing the tumor microvasculature with a nonlinear plane-wave Doppler imaging scheme based on amplitude modulation, *IEEE Trans. Ultrason. Ferroelectr. Freq. Control* **35**, 699 (2015).

[15] J. Yan, B. Huang, J. Tonko, M. Toulemonde, J. Hansen-Shearer, Q. Tan, K. Riemer, K. Ntagiantas, R. Chowdhury, P. Lambiase, R. Senior, and M.-X. Tang, Transthoracic super-resolution ultrasound localisation microscopy of myocardial vasculature in patients, *Nat. Biomed. Eng.* **8**, 689 (2024).

[16] J. Huijssen, *Modeling of nonlinear medical diagnostic ultrasound*, Ph.D. Thesis, Delft University of Technology, 2008.

[17] J. Huijssen and M. D. Verweij, An iterative method for the computation of nonlinear, wide-angle, pulsed acoustic fields of medical diagnostic transducers, *J. Acoust. Soc. Am.* **127**, 33 (2010).

[18] L. Demi, *Modeling nonlinear propagation of ultrasound through inhomogeneous biomedical media*, Ph.D. Thesis, Delft University of Technology, 2013.

[19] L. Demi, K. W. A. van Dongen, and M. D. Verweij, A contrast source method for nonlinear acoustic wave fields in media with spatially inhomogeneous attenuation, *J. Acoust. Soc. Am.* **129**, 1221 (2011).

[20] A. Matalliotakis, D. Maresca, and M. D. Verweij, Nonlinear interaction of two cross-propagating plane waves, arXiv (2023).

[21] A. Matalliotakis and M. D. Verweij, Computation of ultrasound propagation in a population of nonlinearly oscillating

- microbubbles including multiple scattering, *J. Acoust. Soc. Am.* **153**, 2209 (2023).
- [22] T. Segers, E. Gaud, M. Versluis, and P. Frinking, High-precision acoustic measurements of the nonlinear dilatational elasticity of phospholipid coated monodisperse microbubbles, *Soft Matter* **14**, 9550 (2018).
- [23] V. Perrot, M. Polichetti, F. Varray, and D. Garcia, So you think you can DAS? A viewpoint on delay-and-sum beamforming, *Ultrasonics* **111**, 106309 (2021).
- [24] D. Garcia, in *IEEE Int. Ultrason. Symp.* (IEEE, Virtual, 2021).
- [25] T. Lai, M. Bruce, and M. Averkiou, Modeling of the acoustic field produced by diagnostic ultrasound arrays in plane and diverging wave modes, *IEEE Trans. Ultrason. Ferroelectr. Freq. Control* **66**, 1158 (2019).
- [26] R. Hurt, M. Buss, M. Duan, K. Wong, M. You, D. Sawyer, M. Swift, P. Dutka, P. Barturen-Larrea, D. Mittelstein, Z. Jin, M. Abedi, A. Farhadi, R. Deshpande, and M. G. Shapiro, Genomically mined acoustic reporter genes for real-time in vivo monitoring of tumors and tumor-homing bacteria, *Nat. Biotech.* **41**, 919 (2023).
- [27] M. Averkiou, in *IEEE Int. Ultrason. Symp.* (IEEE, San Juan, PR, USA, 2000), pp. 1563–1572.
- [28] C.-C. Shen, Y.-H. Chou, and P.-C. Li, Pulse inversion techniques in ultrasonic nonlinear imaging, *J. Med. Ultrasound* **13**, 3 (2005).
- [29] B. Heiles, A. Chavignon, A. Bergel, V. Hingot, H. Serroune, D. Maresca, S. Pezet, M. Pernot, M. Tanter, and O. Couture, Volumetric ultrasound localization microscopy of the whole rat brain microvasculature, *IEEE Open Trans. Ultrason. Ferroelectr. Freq. Control* **2**, 261 (2022).